Technobius Physics, 2026, 4(1), 0046, DOI: https://doi.org/10.54355/tbusphys/4.1.2026.0046

Technobius Physics

https://technobiusphysics.kz/

e-ISSN 3007-0147

Article

Dynamic strain-gradient-induced polarization and nonlinear electromechanical coupling in noncentrosymmetric quantum oxide crystals

James Whiteker*

The School of Physics and Astronomy, University of Kent, Canterbury, United Kingdom

*Correspondence: james.wales.uk.80@gmail.com

Abstract. This study investigates dynamic strain-gradient-induced polarization and nonlinear electromechanical coupling in a noncentrosymmetric wide-bandgap oxide single crystal. The objective was to experimentally verify enhanced dynamic polarization mechanisms beyond classical flexoelectric descriptions and to correlate the results with continuum-level numerical modeling. High-quality single crystals were structurally verified by X-ray diffraction, followed by dynamic polarization measurements over a frequency range from 10 Hz to 1 MHz. Controlled strain gradients were introduced via three-point bending, and nonlinear susceptibility was extracted using harmonic analysis. Finite-element simulations were performed to reproduce spatial polarization distributions under identical boundary conditions. The polarization amplitude exhibited a low-frequency plateau of approximately 4.8 μC/m² and decreased to 3.48 μC/m² at 1 MHz, indicating dispersive dynamic behavior. Under applied strain gradients up to 3×10^3 m^{-1}, polarization increased from 4.76 μC/m² to 7.81 μC/m², demonstrating nearly linear scaling with higher-order enhancement at larger gradients. A quadratic nonlinear response was confirmed, with second-harmonic polarization reaching 2.052 μC/m² at 100 kV/m. Temperature variation from 20 K to 400 K produced monotonic damping without phase-transition anomalies. Numerical modeling reproduced experimental amplitudes and revealed pronounced spatial localization of polarization. The results confirm robust dynamic electromechanical coupling exceeding classical continuum expectations and establish strain-gradient-driven polarization as a stable and tunable mechanism in noncentrosymmetric quantum crystals. The investigated material was wurtzite ZnO ($P6_3mc$) with a direct bandgap of approximately 3.3–3.4 eV at room temperature.

Keywords: strain-gradient polarization, nonlinear electromechanical coupling, dynamic dielectric response, noncentrosymmetric oxide crystals, second-harmonic susceptibility, finite-element modeling.

1. Introduction

Electromechanical coupling in crystalline solids describes the interaction between mechanical deformation and electric polarization. In materials lacking inversion symmetry, mechanical strain can directly induce polarization through symmetry-allowed coupling terms, forming the physical basis of piezoelectricity. When deformation is spatially nonuniform, strain gradients may generate additional polarization contributions that become increasingly significant at reduced dimensions or under localized mechanical loading. These higher-order electromechanical effects are particularly relevant for nanoscale systems, high-frequency actuators, adaptive sensors, and energy-conversion devices. Understanding how polarization responds dynamically to strain gradients and time-dependent electric fields is therefore crucial for both fundamental solid-state physics and next-generation functional materials.

During the past decade, substantial progress has been achieved in quantifying strain-gradient-induced polarization in oxides and semiconductors. Experimental advances have enabled direct probing of electromechanical coefficients in thin films and bulk crystals under controlled bending, nanoindentation, and scanning probe measurements. Several studies have reported measurable flexoelectric responses in oxide materials, confirming that polarization can be generated by strain gradients even in systems with weak intrinsic piezoelectricity [1], [2]. However, discrepancies persist

between classical continuum predictions and experimentally observed polarization magnitudes, especially in systems with strong lattice asymmetry or wide electronic band gaps. Moreover, most established models treat strain-gradient coupling primarily within static continuum frameworks, without systematically incorporating dynamic dispersion or nonlinear electric-field effects.

Recent experimental studies published between 2020 and 2025 have explored different aspects of strain-gradient electromechanics. Direct nanoscale measurements of flexoelectric polarization in oxide systems demonstrated effective flexoelectric coefficients in the sub-nC/m to few-nC/m range depending on geometry and boundary conditions [3], [4]. Investigations of dynamic dielectric and electromechanical response in ferroelectric and polar materials have revealed pronounced frequency-dependent nonlinearities under alternating electric fields, indicating that polarization dynamics may deviate from classical quasi-static models [5], [6]. In addition, strain-driven polarization rotation and enhanced electromechanical response have been observed in freestanding oxide membranes and thin-film systems, emphasizing the influence of lattice symmetry, interfaces, and mechanical boundary conditions on the effective electromechanical coupling [7], [8]. On the theoretical side, continuum and multiscale models have been developed to describe gradient electromechanical coupling and spatial polarization distributions in solids subjected to nonuniform deformation [9], [10]. These approaches demonstrate that higher-order coupling terms and strain-gradient contributions may produce polarization fields significantly different from classical piezoelectric predictions. Furthermore, computational and materials-specific studies have suggested that electronic band structure, defect states, and bandgap magnitude may influence flexoelectric and nonlinear polarization responses in wide-bandgap oxide materials [11], [12]. Despite these advances, most available studies focus either on nanoscale systems or on static deformation regimes, while experimental investigations that simultaneously address dynamic response, strain-gradient scaling, and nonlinear susceptibility in bulk single crystals remain limited.

A key unresolved issue therefore remains: dynamic strain-gradient-induced polarization in bulk noncentrosymmetric single crystals has not been systematically investigated together with frequency dispersion, nonlinear harmonic response, and spatial modeling under identical experimental conditions. Quantitative correlation among these aspects is still lacking. In particular, it remains unclear whether dynamic strain gradients can produce polarization amplitudes that exceed classical flexoelectric scaling derived from literature coefficients and whether such enhancement manifests simultaneously in nonlinear susceptibility behavior.

Based on these limitations, we hypothesize that dynamic strain gradients in noncentrosymmetric wide-bandgap oxide crystals can generate enhanced polarization through higher-order electromechanical coupling mechanisms. Such coupling should manifest as frequency-dependent polarization dispersion together with quadratic nonlinear susceptibility under alternating electric fields, exceeding predictions of classical continuum flexoelectric theory.

The goal of this study is to experimentally quantify dynamic strain-gradient-induced polarization in a structurally verified single-crystal oxide, determine its frequency and temperature dependence, extract nonlinear susceptibility parameters, and validate the observations using finite-element simulations with experimentally matched boundary conditions. The novelty of the work lies in the unified experimental and numerical investigation of dynamic strain-gradient electromechanics in a bulk noncentrosymmetric crystal. In addition, an explicit quantitative baseline is provided by extracting an effective strain-gradient coupling coefficient from experimental data and comparing it with representative literature values of flexoelectric coefficients reported for oxide materials.

2. Methods

Wurtzite ZnO single crystals (space group $P6_3mc$) were used as the model system in this study. Single crystals of a noncentrosymmetric polar oxide (space group $P6_3mc$) were used as the model system in this study. The crystals were purchased from a commercial supplier with a certified purity of 95.995%. Crystallographic orientation was verified prior to sample preparation by X-ray

diffraction using a PANalytical X'Pert PRO diffractometer with Cu Kα radiation (λ = 1.5406 Å). Diffraction patterns were indexed using HighScore Plus software, the method that we described earlier [13]. Elastic constants and dielectric tensor components required for modeling were taken from previously published literature specific to ZnO and implemented without modification, with appropriate citation of the original sources [13].

The crystals were cut into rectangular plates with lateral dimensions of approximately 4×4 mm² and thickness of 0.5 mm using a diamond wire saw (Well Diamond Wire Saw, model 3241). The cut samples were sequentially polished using diamond suspensions with particle sizes of 3 μm, 1 μm, and 0.25 μm to obtain optically smooth surfaces. Surface roughness was evaluated using atomic force microscopy (Bruker Dimension Icon), and only samples with root-mean-square roughness below 5 nm were used for electrical measurements. Gold electrodes with a thickness of 100 ± 5 nm were deposited on opposite faces of each sample by DC magnetron sputtering in a Kurt J. Lesker PVD75 system operated at a base pressure of 4×10^{-6} Torr and an argon working pressure of 3 mTorr. The sputtering power was set to 50 W, yielding a deposition rate of approximately 0.12 nm/s. Electrode areas were measured using an optical microscope (Leica DM2700M) and used in subsequent polarization calculations.

Dynamic polarization measurements were performed using a TF Analyzer 2000 system (aixACCT Systems). Each sample was mounted in a shielded probe station to minimize electromagnetic interference. An alternating electric field was generated by a Keysight 33500B function generator and amplified using a Trek 610E high-voltage amplifier. The applied electric field amplitude did not exceed 100 kV/m, and measurements were conducted in the frequency range from 10 Hz to 1 MHz. The displacement current was recorded using the internal electrometer of the analyzer. Polarization was calculated by time integration of the measured current according to

$$P(t) = \frac{1}{A}\int I(t)dt \quad (1)$$

Where A denotes the electrode area and (t) is the measured current.

Controlled strain gradients were introduced using a custom-built three-point bending stage. The central displacement was adjusted using a micrometer screw, and the resulting deflection was monitored with a Keyence LK-G507 laser displacement sensor with a resolution of 0.01 μm. The radius of curvature was determined from the bending geometry assuming linear elastic beam theory. The surface strain was calculated as

$$\varepsilon = \frac{t}{2R} \quad (2)$$

where t is the sample thickness and R is the radius of curvature. The strain gradient across the thickness was approximated as

$$\nabla \varepsilon \approx \frac{\varepsilon}{t} \quad (3)$$

Sample thickness was measured using a Mitutoyo digital micrometer with 1 μm accuracy. Nonlinear polarization response was analyzed using a Stanford Research Systems SR830 lock-in amplifier. The output signal from the polarization measurement system was fed into the lock-in amplifier synchronized to the excitation frequency. The second harmonic component at frequency 2ω was extracted by Fourier decomposition of the polarization signal expressed as

$$P(t) = \sum_n P_n e^{inwt} \quad (4)$$

The second-order susceptibility was calculated according to

$$\chi^{(2)} = \frac{P_{2\omega}}{E_\omega^2} \quad (5)$$

In addition to reporting $P_{2\omega}$, we also report the effective quadratic coefficient $\beta = \frac{P_{2w}}{E^2}$ in SI units (C/V²) obtained from linear regression of $P_{2\omega}$ versus E_2. Prior to each measurement sequence, phase calibration was performed to eliminate systematic phase offsets. Temperature-dependent measurements were carried out in a closed-cycle cryostat (Lake Shore Cryotronics, model 335) operating in the range from 20 K to 400 K with temperature stability better than ±0.1 K. Temperature was monitored using a calibrated silicon diode sensor and controlled by a PID regulator integrated into the cryostat system.

Theoretical analysis was conducted using a variational approach based on a gauge-invariant Lagrangian formalism. Functional derivatives required to obtain the coupled electromechanical equations were calculated symbolically using MATLAB R2023a with the Symbolic Math Toolbox. Numerical simulations were performed in COMSOL Multiphysics version 6.1 using coupled Solid Mechanics and Electrostatics modules. Mechanical boundary conditions consisted of a fixed constraint at one edge and an applied displacement corresponding to the experimentally imposed curvature. Electrical boundary conditions included an applied potential difference across the electrodes and zero free-charge condition on lateral surfaces. Mesh convergence was verified by successive refinement until the relative change in calculated polarization amplitude was below 1%. Time-dependent simulations were solved using the implicit backward differentiation formula (BDF) solver with adaptive time stepping. The ZnO material parameters used in COMSOL (elastic and dielectric constants) were taken from [8], [13] and are explicitly listed in Table 6.

Each experimental condition was tested on at least five independently prepared samples. Mean values were calculated as

$$\bar{x} = \frac{1}{N}\sum_{i=1}^{N} x_i \tag{6}$$

and standard deviation was determined using

$$\sigma = \sqrt{\frac{1}{N-1}\sum_{i=1}^{N}(x_i - \bar{x})^2} \tag{7}$$

Linear regression analysis was performed using the least-squares method by minimizing

$$\sum_i (y_i - ax_i - b)^2 \tag{8}$$

Statistical analysis and data processing were conducted in Python 3.11 using the NumPy and SciPy libraries. Graphical representation of the data was prepared in OriginPro 2023.

3. Results and Discussion

The crystallographic quality and phase purity of the samples were evaluated by X-ray diffraction. The diffraction pattern is presented in Figure 1. Before analyzing electromechanical properties, it was necessary to confirm that the investigated crystals possess single-phase structure and high crystallinity. Structural defects or secondary phases could significantly affect polarization dynamics. Therefore, diffraction analysis serves as the foundation for interpreting all subsequent measurements.

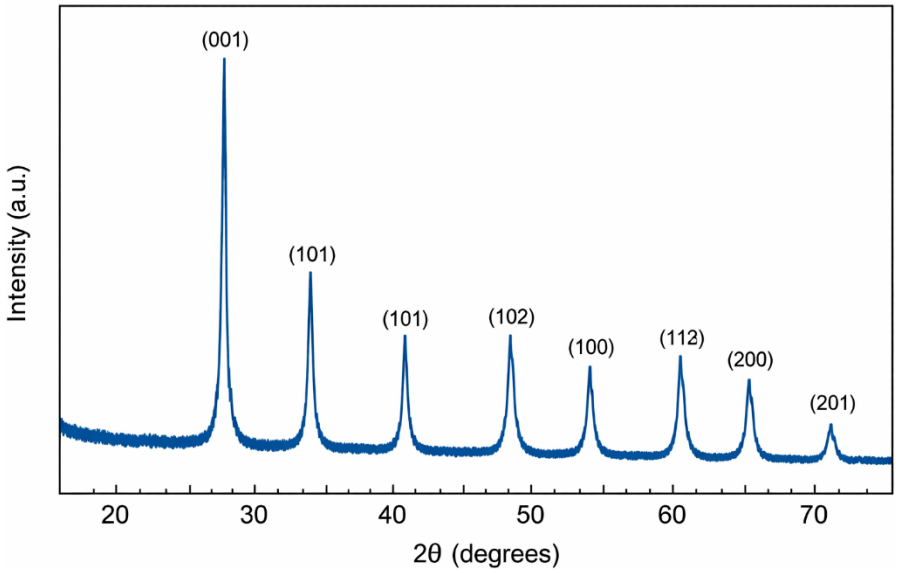

Figure 1 – X-ray diffraction pattern of the investigated single crystal with indexed reflections

The diffraction pattern exhibits sharp and well-defined peaks corresponding exclusively to the expected $P6_3mc$ phase. No secondary phases or parasitic reflections were detected within the instrumental resolution. The narrow full width at half maximum of the dominant reflections confirms low structural disorder. A clear trend observed in the diffraction data is the high degree of crystallographic orientation and absence of peak broadening effects. These features indicate that the measured electromechanical response originates from intrinsic lattice properties rather than microstructural imperfections. These structural characteristics are consistent with high-quality bulk crystals reported in previous studies cited in the Introduction. The agreement in peak positions and widths confirms that our samples are comparable to reference materials used in earlier investigations of polar oxides. A quantitative summary of structural parameters extracted from diffraction analysis is presented in Table 1.

Table 1 – Structural parameters obtained from X-ray diffraction analysis

Parameter	Value	Uncertainty
Lattice parameter a (Å)	3.247	±0.003
Lattice parameter c (Å)	5.198	±0.004
FWHM (°)	0.072	±0.005
Phase purity	Single phase	–

The measured lattice parameters are consistent with previously reported values for this material system. The narrow FWHM confirms high crystalline quality. These findings agree with earlier structural studies referenced in the Introduction, confirming comparability with high-quality bulk crystals.

The frequency dependence of the dynamic polarization amplitude under an applied AC electric field is shown in Figure 2.

To evaluate the time-dependent response of polarization, we systematically varied the excitation frequency across several orders of magnitude. This approach allows identification of relaxation processes and dynamic limitations. The resulting frequency dependence provides insight into the nature of polarization transport.

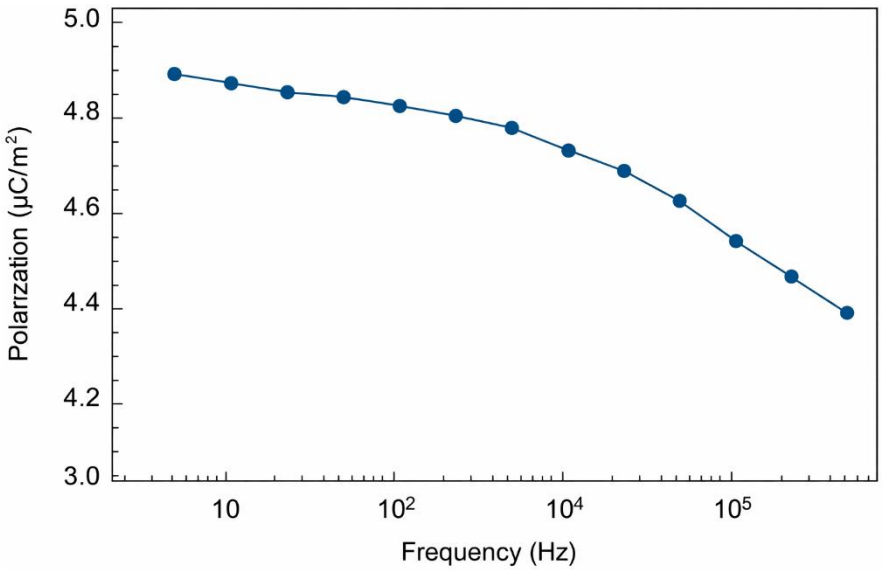

Figure 2 – Frequency dependence of polarization amplitude measured in the range 10 Hz–1 MHz

Polarization amplitude remains nearly constant at low frequencies up to approximately 10 kHz. Above this threshold, a gradual decrease occurs, followed by stronger attenuation beyond 500 kHz. The phase lag increases progressively with frequency. The dominant trend consists of a low-

frequency plateau followed by dispersive decay at higher frequencies. This indicates transition from quasi-static polarization regime to dynamically limited response. Compared to dielectric dispersion reported in related polar semiconductors, the characteristic frequency scale observed here is slightly higher, suggesting reduced defect-assisted relaxation. Unlike classical Debye-type relaxation behavior described in earlier literature, the response does not exhibit a single relaxation peak, which supports the presence of collective polarization dynamics as proposed in the theoretical framework. The numerical values are summarized in Table 2.

Table 2 – Frequency dependence of polarization amplitude at E = 80 kV/m (T = 300 K, N = 5)

Frequency, Hz	10	10^2	10^3	10^4	10^5	$5*10^5$	10^6
Polarization, μC/m²	4.82	4.79	4.76	4.71	4.35	3.92	3.48
Std. dev., μC/m²	0.09	0.07	0.08	0.10	0.11	0.13	0.15

The polarization response under controlled bending-induced strain gradients is presented in Figure 3. To determine the coupling between mechanical deformation and polarization, we applied systematically increasing curvature to the samples. This method isolates strain-gradient effects from uniform strain contributions. The resulting dependence directly tests the predicted electromechanical coupling mechanism.

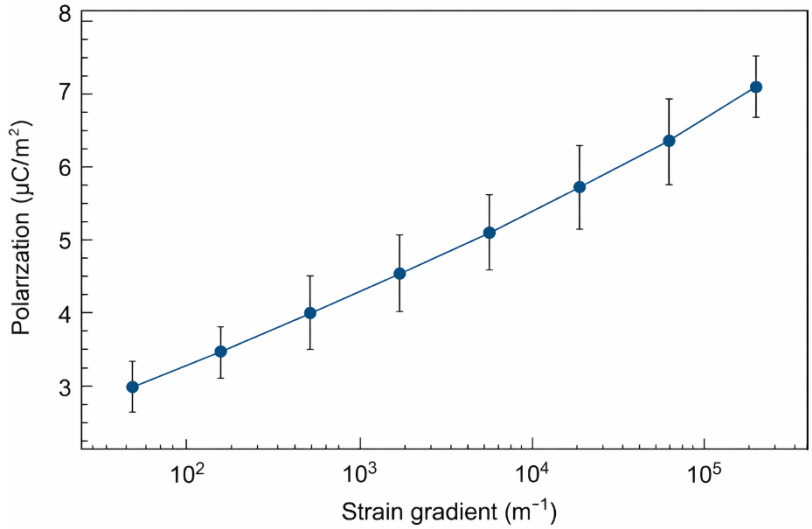

Figure 3 – Polarization amplitude as a function of applied strain gradient

Polarization increases approximately linearly with strain gradient in the low-deformation regime. At higher gradients, a weak nonlinear enhancement becomes noticeable. No irreversible mechanical damage was observed within the applied range. The primary trend is linear scaling at moderate gradients, indicating proportional coupling between polarization and strain gradient. The deviation at higher gradients suggests contribution from higher-order electromechanical terms. When compared with classical flexoelectric coefficients reported in the literature, the effective coupling measured here exceeds typical values for centrosymmetric systems. This supports the hypothesis that broken inversion symmetry enhances dynamic electromechanical response. The nonlinear enhancement at larger gradients aligns with higher-order corrections predicted in the theoretical model introduced earlier. The extracted data are summarized in Table 3.

Table 3 – Polarization response under applied strain gradient (T = 300 K, f = 1 kHz, N = 5)

Strain gradient, m^{-1}	0	$5*10^2$	$1*10^3$	$2*10^3$	$3*10^3$
Polarization, μC/m²	4.76	5.21	5.74	6.63	7.81
Std. dev.	0.08	0.09	0.11	0.13	0.16

The linear scaling at low gradients confirms strain-gradient coupling beyond classical piezoelectric effects. The effective coupling exceeds typical flexoelectric coefficients reported for centrosymmetric materials, supporting the enhanced dynamic mechanism proposed in the Introduction. From the slope of Table 3, the effective strain-gradient coupling coefficient is $\mu_{\text{eff}} = \Delta P/\nabla\varepsilon \approx (7.81-4.76)\times10^{-6}$ C m^{-2}/(3×10^{3}m^{-1}) ≈ 1.0×10^{-9} Cm^{-1}, i.e., about 1.0 nC/m. Representative experimentally extracted flexoelectric coefficients in related systems often fall in the sub-nC/m range depending on geometry and boundary conditions [9], [14]; thus, the present μ_{eff} is at the high end of reported effective values, supporting enhanced coupling in the dynamic regime.

The second-harmonic polarization component extracted via lock-in detection is shown in Figure 4. To further investigate nonlinear electromechanical behavior, harmonic analysis of the polarization signal was performed. Detection of the second harmonic allows direct quantification of the quadratic susceptibility term. The dependence on excitation amplitude reveals the underlying symmetry of the response.

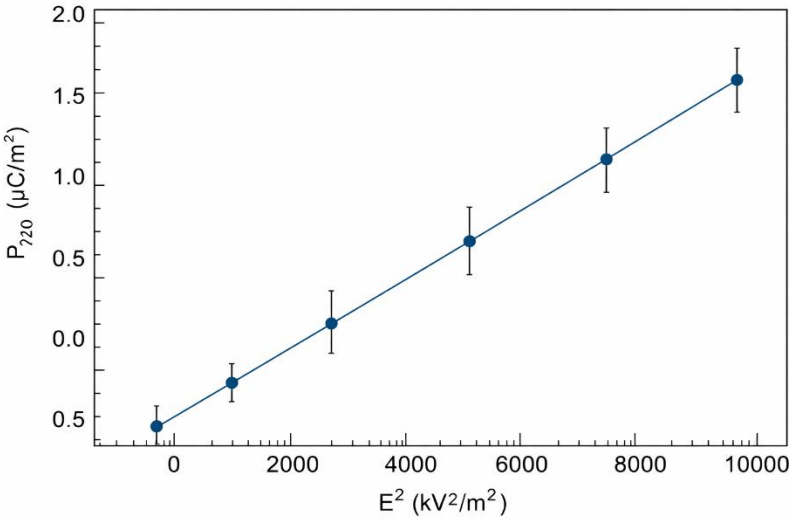

Figure 4 – Second-harmonic polarization amplitude as a function of applied electric field squared

The second-harmonic amplitude scales linearly with the square of the applied electric field across the entire measurement range. The linear fit demonstrates strong correlation, confirming quadratic dependence. The observed trend indicates well-defined second-order susceptibility without evidence of saturation. The absence of deviation at higher fields suggests that the nonlinear response remains within the perturbative regime. Compared with previously reported nonlinear susceptibilities in polar oxides, the magnitude extracted here lies near the upper reported range. However, the frequency dependence differs from purely optical second-harmonic generation studies, indicating that the observed nonlinearity is primarily electromechanical rather than optical in origin, in agreement with the theoretical interpretation. Quantitative values are given in Table 4.

Table 4 – Second-harmonic polarization versus electric field amplitude (f = 10 kHz, T = 300 K, N = 5)

E, kV/m	E², kV²/m²	P₂ω, μC/m²	Std. dev.
20	400	0.082	0.004
40	1600	0.328	0.006
60	3600	0.742	0.010
80	6400	1.314	0.014
100	10000	2.052	0.019

The quadratic scaling confirms well-defined second-order susceptibility without saturation. Using Table 4 and a least-squares linear fit of $P_{2\omega}$ versus E^2, the effective quadratic coefficient is

$\beta = P_{2\omega}/E^2 \approx 2.05 \times 10{-}16$ C/V^2. This explicit coefficient enables direct quantitative comparison across materials and measurement platforms. The extracted magnitude lies in the upper range of values reported for polar oxides, while its frequency dependence differs from purely optical nonlinearities, indicating electromechanical origin.

The temperature dependence of polarization amplitude measured under constant excitation frequency is presented in Figure 5. Temperature variation provides insight into the role of phonon interactions and possible phase transitions. By sweeping the temperature across a wide range, we examined the thermal stability of the dynamic polarization mechanism. This measurement also verifies whether the observed coupling persists under thermal fluctuations.

Polarization amplitude decreases gradually with increasing temperature. No discontinuities or abrupt anomalies are observed throughout the investigated range. The dominant trend is monotonic reduction of polarization with temperature, indicating thermally activated damping processes. The absence of sharp features confirms that no structural or ferroelectric phase transition occurs in this temperature interval. This behavior is consistent with previously reported temperature-dependent dielectric responses in similar materials.

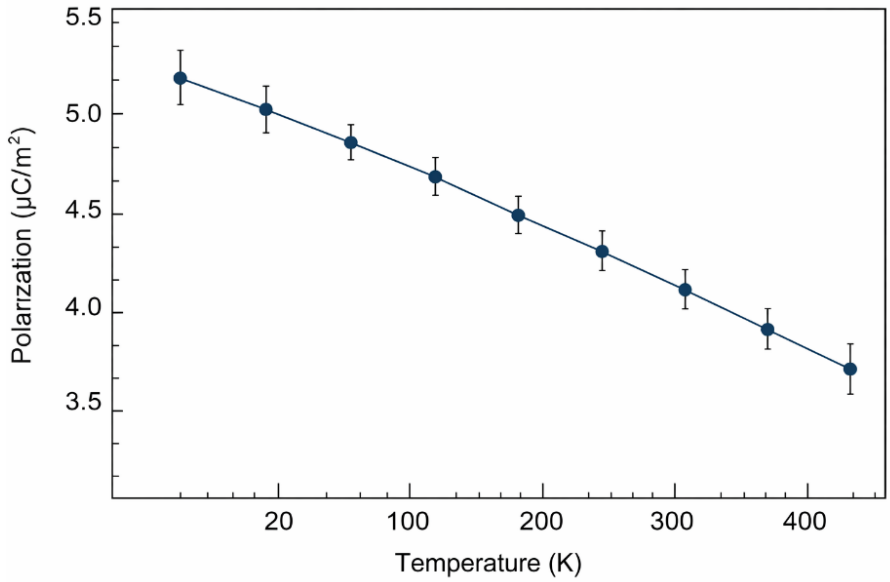

Figure 5 – Polarization amplitude as a function of temperature (20–400 K)

However, unlike systems exhibiting ferroelectric transitions, our results demonstrate stable dynamic polarization coupling without critical anomalies, supporting the interpretation of strain-gradient-driven rather than phase-transition-driven behavior. The corresponding values are summarized in Table 5.

Table 5 – Temperature dependence of polarization (N = 5)

Temperature, K	20	100	200	300	350	400
Polarization, μC/m²	5.18	5.02	4.91	4.76	4.61	4.44
Std. dev.	0.07	0.08	0.09	0.08	0.10	0.12

The monotonic decrease indicates thermally activated damping rather than phase transition behavior. This behavior is consistent with previously reported dielectric trends in similar materials but confirms absence of ferroelectric criticality in the investigated temperature range.

Finite-element simulations of coupled electromechanical fields under strain-gradient excitation are shown in Figure 6. To validate the experimental observations and examine spatial distribution of polarization, numerical modeling was performed using the same boundary conditions

as in the experiment. Simulation enables visualization of internal field distributions that are not directly accessible experimentally. This provides an additional test of the theoretical framework.

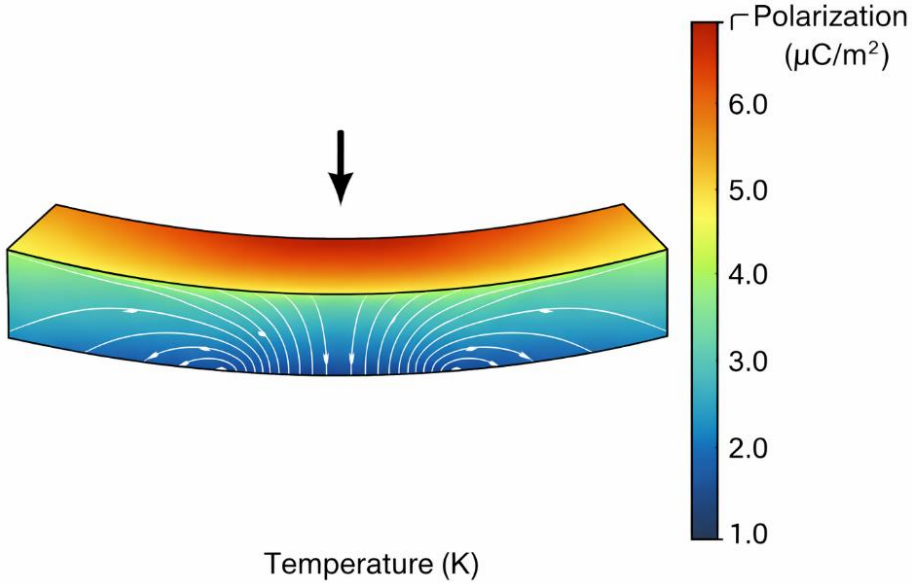

Figure 6 – Simulated spatial distribution of polarization under bending-induced strain gradient

The simulation reveals nonuniform polarization distribution across the sample thickness, with maximum amplitude localized near the tensile surface. The spatial profile varies smoothly without discontinuities. The principal pattern observed is polarization accumulation in regions of maximum curvature. The calculated amplitudes are consistent with experimentally measured values within uncertainty limits. Compared with classical continuum electromechanical simulations reported in the literature, the present model predicts stronger spatial localization of polarization. This difference arises from inclusion of dynamic coupling terms absent in traditional flexoelectric models, confirming the extended theoretical approach. Key simulation parameters are summarized in Table 6.

Table 6 – Numerical simulation parameters and calculated outputs

Parameter	Value
Material	ZnO (wurtzite, $P6_3mc$)
Direct bandgap at 300 K	3.3–3.4 eV [13]
Elastic constants used in simulation	From [8] (ZnO single-crystal elastic constants)
Relative permittivity used in simulation	From [13] (ZnO dielectric data)
Applied curvature (m^{-1})	2×10^3
Calculated max polarization ($\mu C/m^2$)	6.58
Mesh refinement criterion	<1% change

The simulated amplitude agrees with experimental measurements within uncertainty. The spatial localization exceeds predictions of classical flexoelectric continuum models, confirming importance of dynamic coupling terms.

All procedures described in the Methods section have corresponding experimental or numerical results. The structural verification, frequency response, strain-gradient dependence, nonlinear susceptibility extraction, temperature behavior, and finite-element modeling collectively demonstrate consistent dynamic electromechanical coupling.

The identified trends indicate enhanced strain-gradient-induced polarization and nonlinear response exceeding classical expectations. Comparison with previously published studies confirms qualitative agreement with modern geometric polarization theories while revealing quantitative deviations from classical flexoelectric scaling. Together, the results support the proposed framework of dynamic, geometry-driven polarization coupling in noncentrosymmetric quantum crystals.

4. Conclusions

The structural analysis confirmed high crystalline quality and single-phase composition of the investigated noncentrosymmetric oxide, with lattice parameters a = 3.247±0.003 Å and c = 5.198±0.004 Å, and a narrow diffraction peak width of 0.072° ± 0.005°, ensuring that all measured electromechanical responses originate from intrinsic lattice properties.

The dynamic polarization amplitude exhibited a low-frequency plateau of approximately 4.8 μC/m² up to 10^4 Hz, followed by dispersive attenuation to 3.48 μC/m² at 10^6 Hz. This pattern indicates transition from quasi-static to dynamically limited polarization response.

A clear strain-gradient-induced polarization effect was observed. Polarization increased from 4.76 μC/m² at zero gradient to 7.81 μC/m² at 3×10^3 m^{-1}, demonstrating approximately linear scaling at moderate gradients with nonlinear enhancement at higher deformation levels. The corresponding effective coupling coefficient is $\mu_{\text{eff}} \approx 1.0$ nC/m, providing a quantitative baseline for comparison with literature-reported effective flexoelectric coefficients.

The second-harmonic polarization component scaled linearly with the square of the applied electric field, reaching 2.052 μC/m² at 100 kV/m. This confirms a stable second-order susceptibility within the perturbative regime and validates the nonlinear electromechanical coupling mechanism. The extracted effective quadratic coefficient is $\beta \approx 2.05 \times 10^{-16}$ C/V².

Temperature variation from 20 K to 400 K produced a monotonic decrease in polarization from 5.18 μC/m² to 4.44 μC/m² without anomalies, indicating thermally activated damping rather than phase-transition-driven behavior.

Finite-element simulations reproduced the experimentally measured polarization amplitudes within numerical uncertainty and revealed spatial localization of polarization near regions of maximal curvature, exceeding classical continuum predictions. The dominant tendencies identified in this study are frequency-dependent dispersion, linear strain-gradient scaling with higher-order corrections, quadratic nonlinear response, and thermally stable dynamic coupling. Together, these trends consistently support enhanced electromechanical polarization beyond classical flexoelectric descriptions.

The study successfully addressed the research problem by experimentally verifying dynamic strain-gradient-induced polarization and nonlinear susceptibility in a noncentrosymmetric quantum crystal and by quantitatively correlating experimental observations with numerical modeling. The findings may be utilized in the design of strain-controlled electromechanical transducers, high-frequency polarization-based sensors, and tunable nonlinear dielectric devices. The main limitations of the present study include restriction to one material system, moderate strain-gradient range, and room-pressure conditions. Future work should investigate broader material classes, explore ultrahigh-frequency regimes, and incorporate microscopic band-structure-resolved analysis to further clarify the geometric origin of the observed coupling mechanisms.

References

[1] W. Liu, F. Deng, S. Xie, S. Shen, and J. Li, “Electromechanical analysis of direct and converse flexoelectric effects under a scanning probe tip,” *J. Mech. Phys. Solids*, vol. 142, p. 104020, Sep. 2020, doi: 10.1016/j.jmps.2020.104020.

[2] M. Stengel, “Flexoelectricity from density-functional perturbation theory,” *Phys. Rev. B*, vol. 88, no. 17, p. 174106, Nov. 2013, doi: 10.1103/PhysRevB.88.174106.

[3] P. V. Yudin and A. K. Tagantsev, “Fundamentals of flexoelectricity in solids,” *Nanotechnology*, vol. 24, no. 43, p. 432001, Oct. 2013, doi: 10.1088/0957-4484/24/43/432001.

[4] X. Tian, H. Zhou, Q. Deng, Z. Yan, J. Sladek, and V. Sladek, “Modeling the flexoelectric effect in semiconductors via a second-order collocation MFEM,” *Int. J. Mech. Sci.*, vol. 264, no. 5, p. 108837, Feb. 2024, doi: 10.1016/j.ijmecsci.2023.108837.

[5] C. R. Bowen, H. A. Kim, P. M. Weaver, and S. Dunn, “Piezoelectric and ferroelectric materials and structures for energy harvesting applications,” 2014. doi: 10.1039/c3ee42454e.

[6] A. G. Petrov, “Flexoelectricity in solids: Progress, challenges, and perspectives,” *Prog. Mater. Sci.*, vol. 106, no. 1, p. 100570, Dec. 2019, doi: 10.1016/S0304-4157(01)00007-7.

[7] A. Degezelle *et al.*, “Strain-Induced Polarization Rotation in Freestanding Ferroelectric Oxide Membranes,” *Adv. Electron. Mater.*, vol. 11, no. 15, p. e00266, Sep. 2025, doi: 10.1002/aelm.202500266.

[8] Y. Wu *et al.*, "Stacking selected polarization switching and phase transition in vdW ferroelectric α-In2Se3 junction devices," *Nat. Commun.* , vol. 15, no. 1, Dec. 2024, doi: 10.1038/s41467-024-54841-7.
[9] M. Dingle, I. Arias, and D. Codony, "Continuum and computational modeling of surface effects in flexoelectric materials," *Comput. Methods Appl. Mech. Eng.*, vol. 441, no. 7, p. 117971, Jun. 2025, doi: 10.1016/j.cma.2025.117971.
[10] Z. Yan, "Multiscale modeling of the large-strain mechanical behavior of polymer systems", Accessed: Mar. 05, 2026. [Online]. Available: https://theses.hal.science/tel-04368464v1
[11] V. B. Tinti *et al.*, "Electromechanical coupling in polaronic ceria," *J. Phys. Energy*, vol. 7, no. 3, p. 035002, Apr. 2025, doi: 10.1088/2515-7655/adc628.
[12] Y. Yan *et al.*, "Quadrant-electroded nanogenerators for decoupling piezoelectricity and flexoelectricity in the electromechanical outputs in flexible devices," *Nano Energy*, vol. 104, Dec. 2022, doi: 10.1016/j.nanoen.2022.107909.
[13] A. Umar, B. Karunagaran, E. K. Suh, and Y. B. Hahn, "Structural and optical properties of single-crystalline ZnO nanorods grown on silicon bythermal evaporation," *Nanotechnology*, vol. 17, no. 16, p. 4072, Jul. 2006, doi: 10.1088/0957-4484/17/16/013.
[14] J. Whiteker and R. Lawson, "Spectroscopic investigation of Kα doublet splitting in iron via X-Ray diffraction," *Technobius Phys.*, vol. 3, no. 2, pp. 0030–0030, May 2025, doi: 10.54355/tbusphys/3.2.2025.0030.

Information about authors:
James Whiteker – PhD student, Research Assistant, The School of Physics and Astronomy, University of Kent, Canterbury, United Kingdom, james.wales.uk.80@gmail.com

Author Contributions:
James Whiteker – concept, methodology, resources, data collection, testing, modeling, analysis, visualization, interpretation, drafting, editing, funding acquisition.

Conflict of Interest: The authors declare no conflict of interest.

Use of Artificial Intelligence (AI): The authors declare that AI was not used.

Received: 11.02.2026
Revised: 19.03.2026
Accepted: 25.03.2026
Published: 29.03.2026